

pubs.acs.org/cm Article

Colloidal Stability and Solubility of Metal—Organic Framework Particles

Michael A. LeRoy, Anton S. Perera, Shasanka Lamichhane, Ashley N. Mapile, Faiqa Khaliq, Kentaro Kadota, Xianghui Zhang, Su Ha, Racheal Fisher, Di Wu, Chad Risko, and Carl K. Brozek*



Cite This: Chem. Mater. 2024, 36, 3673-3682



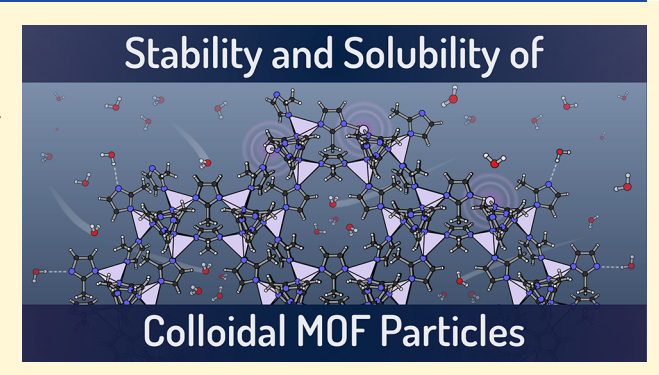
ACCESS I

Metrics & More

Article Recommendations

Supporting Information

ABSTRACT: Chemical separation membranes, drug delivery agents, and other nascent applications of metal—organic frameworks (MOFs) benefit from preparing MOFs as nanoparticles (nano-MOFs) and by controlling their particle surfaces. Despite the lack of deliberately added surface ligands, or surfactants, common examples of nanoMOFs exhibit multiweek colloidal stability in a range of polar solvents. Whereas nanocrystal colloidal stability in general arises from a combination of electrostatic repulsion, steric hindrance between surface species, and favorable interactions with solvent, nanoMOFs present the unusual combination of interior and exterior surfaces for these interactions to transpire. Here, we demonstrate that nanoMOFs suspend only in solvents that dissolve the constituent MOF linkers. Moreover, the maximum "solubility" of



nanoMOFs, i.e., the concentration of saturated particle suspensions, correlates with the solubility of the linkers in the same solvent. Calorimetry measurements indicate that nanoMOF immersion enthalpies resemble the solvation enthalpies of the linkers, suggesting solvent—linker interactions dictate nanoMOF colloidal stability. As a proof-of-concept, whereas nanoMOFs generally suspend only in polar solvents, we achieve nanoMOF suspensions in toluene by identifying linkers soluble in the same solvent. Furthermore, atomistic molecular dynamics simulations reveal that solvents best at dissolving nanoMOFs are those that pack densely into the pores and interact with the MOF linkers. These results provide a predictive tool for achieving nanoMOF colloidal stability and highlight the uniqueness of defining a MOF "surface", where solvents access both interior and exterior surfaces.

■ INTRODUCTION

Colloidal nanoparticles have reshaped materials science by combining solution processability with size-dependent behavior. Due to their large surface-to-volume ratios, colloidal nanoparticles are defined by their surface chemistry for both practical and fundamental considerations: colloidal stability, particle self-assembly,^{2,3} interfacial electrochemical phenomena, surface plasmon resonances, photophysical dynamics, heterogeneous reactivity, and interparticle energy transfer⁵ represent just a few of the fundamental areas governed by nanoparticle surfaces. Careful tuning of surface composition is also key to many practical goals: solution processability, interfacing nanocrystal into composite materials,6 and achieving environmental stability and biocompatibility. Given that this research derives from a relatively small subset of materials—namely metals and conventional semiconductors, such as metal chalcogenides—a major outstanding goal is to prepare other classes of nanomaterials with intrinsically distinct behavior.

Metal-organic frameworks (MOFs) have been targeted for a wide range of fundamental questions and practical applications due to their porosity and wide synthetic tunability. Recent studies indicate their practical implementation in membrane-based applications requires the preparation of MOFs as nanoparticles rather than as bulk powder, ^{8,9} in part to enable control over particle size and morphology, and to enhance their biocompatibility ¹⁰ and solution processability. ¹¹ Few MOFs have been prepared as nanoparticles, however. In the scarce existing synthetic methods, "modulators", rather than the typical surfactant ligands found in the quantum dot literature, direct the size of MOF nanoparticles (nano-MOFs). ¹² Unlike surfactant ligands, evidence suggests that modulators only rarely incorporate onto the exterior or interior surfaces. ^{13–15} Instead, as described by the "seesaw" model reported previously, modulators influence particle sizes by affecting the metal—linker binding and linker deprotonation equilibria. ^{12,16} With this predictive model, we recently

Received: December 14, 2023 Revised: April 1, 2024 Accepted: April 2, 2024 Published: April 11, 2024





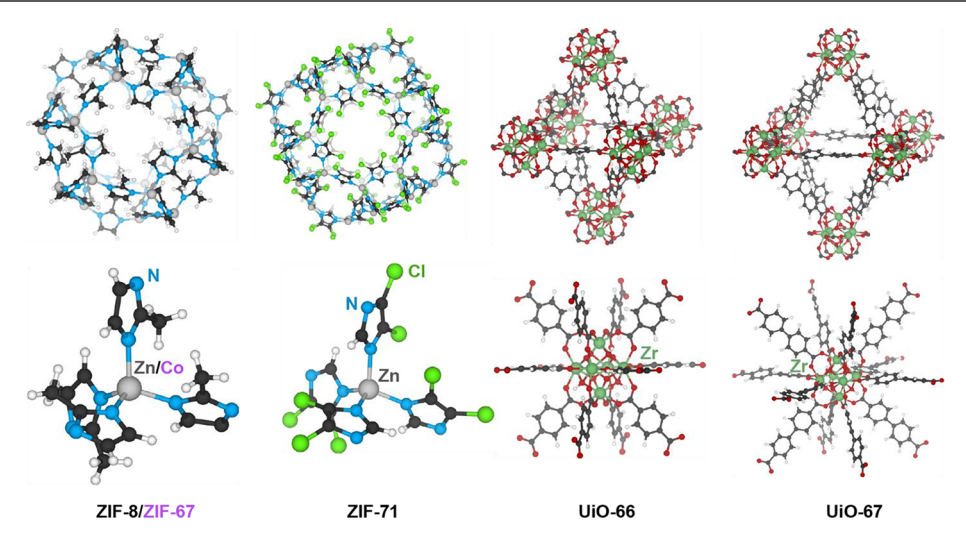


Figure 1. Crystallographic images of the metal—organic framework materials investigated by solubility measurements, with representative pore apertures (top) and corresponding metal—ion environment (bottom) highlighted.

demonstrated a nanoparticle synthesis of the conductive MOF $Fe(1,2,3-triazolate)_2$ with diameter sizes controllable to just 6 nm—the smallest nanoMOFs to-date. 14 Size-dependent optical and charge-transport behavior emerged from this new class of semiconductor nanocrystals distinct from traditional quantum dots. Remarkably, despite the lack of surfactant additives and the absence of incorporated modulator, the particles exhibited indefinite colloidal stability in DMF under anaerobic conditions. Bare particles of nonporous 17 and porous 10,18 inorganic materials have been stabilized through electrostatic repulsion between large surface charge, in accordance with Derjaguin-Landau-Verwey-Overbeek (DLVO) theory. Porous inorganic particles have also been stabilized through non-DLVO-type forces such as through favorable solvent interactions at the nanoparticle external surfaces. 22,23 Unlike these examples, nanoMOFs possess organic constituents with the potential for favorable solvent interactions at both the interior and exterior surfaces, akin to polymers and other soluble macromolecules. In fact, such solvent-linker interactions may resemble those responsible for the stabilization of nonporous nanoparticles coated with organic capping ligands.²⁴ From an applications perspective, the ability to functionalize nanoMOFs into polymer matrices will be impacted by the surface interactions underpinning this unexpected colloidal stability.²⁵⁻²⁸ These fundamental and technological questions therefore motivate a need to understand the structure and composition of nanoMOF surfaces and the nature of their interfacial interactions.

Here, we report the week-long colloidal stability of common nanoMOFs (Figure 1) in the absence of conventional surface ligands. Rather than electrostatic repulsion from surface charges or steric repulsion from surface ligands, colloidal stability appears to arise from interactions between solvent and the particles. We find that the maximum amount of nanoMOFs that may be suspended (particle solubility) correlates with the solubility of the native MOF linker and the ability of solvent to access interior particle surfaces. While altering the metal ion identity leaves particle solubility unchanged, altering linker identity changes particle solubility to correlate with the linker solubility. Furthermore, calorimetry measurements indicate the immersion enthalpies of nanoMOFs resemble the solvation

enthalpies of the constituent linkers and that these energies are independent of particle size. Atomistic molecular dynamics (MD) simulations reveal that solvents best at dissolving nanoMOFs are those that pack densely into the pores and interact with the linkers. Taken together, these results provide a foundation for predicting the best solvents for preparing colloidally stable nanoMOFs. On a fundamental level, these results open opportunities for exploring a fundamentally distinct type of material interface that includes both exterior and interior surfaces, where guest molecules access both and strongly influence colloidal behavior.

EXPERIMENTAL SECTION

Materials. All chemicals were used as purchased unless otherwise stated: zinc(II) nitrate hexahydrate (99%, metal basis, crystalline, Thermo Fisher Scientific), 2-methylimidzole (99%, Acros Organics), zinc(II) acetate dihydrate (crystalline, Baker Analyzed, J.T. Baker), 4,5-dichloroimidazole (98% Beantown Chemical), benzimidazole (Aldrich), titanium(IV) butoxide (TCI Chemicals), 1,4-benzenedicarboxylic acid (terephthalic acid), biphenyl-4,4'-dicarboxylic acid (Chem Scene LLC), benzoic acid (JT Baker), copper(II) nitrate trihydrate (99%, Acros Organics), 1H-1,2,3-triazole (98%, TCI), zirconium(IV) chloride (99.5%, Strem Chemicals), zinc(II) acetate dihydrate (JT Baker), 2,5-dihydroxyterephthalic acid (98% TCI Chemicals), hydrochloric acid (certified ACS Plus, Fisher Chemical), tetrabutylammonium chloride (98% TCI Chemicals), tetrabutylammonium nitrate (98% TCI Chemicals), tetrabutylammonium hexafluorophosphate (98% TCI Chemicals), potassium hexafluorophosphate (>95% TCI Chemicals), cobalt(II) nitrate (anhydrous, Baker Analyzed, J.T. Baker), MeOH (certified ACS, Fisher Chemical), ethanol (200 Proof, anhydrous meets UPS specs, Decon Laboratories Inc.), N,N-dimethylformamide (certified ACS, Fisher Chemical), and Milli-Q water 18.2 M Ω cm⁻¹.

Synthesis of CuTA₂ Nanoparticles. In a 20 mL scintillation vial, 0.059 g of $\text{Cu(NO}_3)_2$:6H₂O was dissolved in 2 mL of DMF. To this solution was added 42.6 μ L of 1H-1,2,3-triazole. The vial was capped and heated at 100 °C for 2 h with stirring, followed by centrifugation and washing with DMF three times.

Synthesis of MIL-125 Nanoparticles. A two-neck round-bottom flask fitted with a reflux condenser and gas adapter was charged with terephthalic acid (0.352 g, 2.12 mmol) and cycled under dynamic vacuum and $\rm N_2$ before being put under a steady flow of $\rm N_2$. Dry DMF (5 mL) was added, then allowed to stir at 110 °C for 30 min. After complete dissolution of the linker, 1.5 mL of MeOH, benzoic acid (1.18 g, 10.6 mmol), and 5 μ L of DI water were added, and the solution was stirred under reflux for an additional 30 min. $\rm Ti(IV)$

butoxide (0.42 mL, 1.23 mmol) was then added and the reaction was stirred vigorously at 110 $^{\circ}$ C under reflux for 14 h. The particles were then washed with cold DMF and then MeOH three times.

Synthesis of 26 nm MOF-74 Nanoparticles. Five mL of a 0.25 M solution of $Zn(OAc_2)\cdot 2H_2O$ (2.29 g, 5 mmol) in EtOH:DMF (1:1) was added to a scintillation vial and stirred. Five milliliters of a 0.1 M 2,5-dihydroxyterephalic acid (0.99 g, 2 mmol) was injected via syringe at a rate of 1 mL/min. After 24 h, the reaction was stopped by centrifugation and washing three times with MeOH.

Synthesis of UiO-66/67 Nanoparticles. A three-neck round-bottom flask fitted with a reflux condenser and gas adapter was charged with terephthalic acid or biphenyl-4,4'-dicarboxylic acid (2.12 mmol) and cycled under dynamic vacuum and N_2 before being put under a steady flow of N_2 . DMF (5 mL) was added, and then the mixture was allowed to stir at 110 °C for 30 min. After complete dissolution of the linker, 5 μ L of DI water were added. Zr(IV) chloride (1.00 g, 1.23 mmol) was then added, and the reaction was stirred vigorously at 110 °C under reflux for 2 h. The particles were then centrifuged and then washed with MeOH three times.

Synthesis of ZIF-8 Nanoparticles. ZIF-8 nanoparticles (nano-ZIF-8) were synthesized following the literature procedure. In general, to synthesize 36 nm nanoZIF-8, zinc nitrate hexahydrate (2.00 g, 6.72 mmol) in 136 mL of MeOH was poured into a 2-methylimidazole solution (2.76 g, 33.6 mmol) in 136 mL of MeOH stirring at 500 rpm and left to react for 1 h. The resulting nanoparticles were centrifuged and washed three times with MeOH by sonication and centrifugation. The particles were then dried at 100 °C under vacuum for 24 h. To achieve different sizes, the ratio of Zn:2Mim:MeOH was adjusted by a scale of 1:x:1000 with x=2, 3, and 5 equiv for large, medium, and small sizes of nanoZIF-8, respectively. SEM images of nanoZIF-8 are shown in Figure S1.

Synthesis of ZIF-71 Nanoparticles. 35 nm. Zinc acetate dihydrate $Zn(OAc_2)\cdot 2H_2O$ (0.11 g, 0.6 mmol) in 5 mL of DMF was combined with 4,5-dichloroimidazole (dcIm, 0.27 g, 2 mmol) in 5 mL of MeOH stirring at 500 rpm. The solution immediately turned a milky pink and was left to react for 45 min. The resulting solution was centrifuged and washed three times with MeOH.

54 nm. $\rm Zn(OAc_2)\cdot 2H_2O$ (0.037 g, 0.2 mmol) in 5 mL of DMF was combined with dcIm (0.11 g, 0.8 mmol) in 10 mL of MeOH stirring at 500 rpm. The solution immediately turned a milky pink and was left to react for 30 min and left static at room temperature for 24 h. The resulting solution was centrifuged and washed three times with MeOH.

83 nm. Zn(OAc₂)·2H₂O (0.037 g, 0.20 mmol) in 5 mL of DMF was combined with dcIm (0.11 g, 0.80 mmol) in 10 mL of MeOH stirring at 500 rpm. A 1-M HCl (2 μ L, 0.00008 mmol) solution was added to the reaction and immediately removed from stirring and left static at room temperature for 24 h. The resulting solution was centrifuged and washed three times with MeOH.

SEM images of nanoZIF-71 are shown in Figure S1.

Synthesis of ZIF-11 Particles. In general, to synthesize ZIF-11, a solution of $Zn(OAc_2)\cdot 2H_2O$ (0.100 g, 0.455 mmol) and 5 mL of NH₄OH (5-M) were added to 5.3 mL of toluene. This solution was poured into a benzimidazole solution (0.120 g, 1.02 mmol) in 50 mL of MeOH stirring at 500 rpm and left to react for 3 h. The resulting nanoparticles were centrifuged and washed three times with MeOH by sonication and centrifugation. The resulting particles were then dried at 100 °C under vacuum.

Powder X-ray Diffraction. Sample crystallinity was verified by powder X-ray diffraction (PXRD) with a Bruker D2 Phaser benchtop diffractometer. Using the PXRD, Scherrer analysis was conducted to analyze crystallite size of the nanoMOFs and are shown in Figures S2–S8.

Dynamic Light Scattering (DLS) and Zeta Potential Measurements. DLS and zeta potential measurements were performed using a Zetasizer Nano from Malvern Panalytical. For the DLS experiments, three measurements were conducted per sample, and for the zeta potential, five measurements were conducted per sample. Before each measurement the sample was sonicated for 10 min to break up any aggregates that had potentially formed.

Solubility Measurements. All samples were prepared by adding excess nanoMOF or linker to 500 μ L or 1 mL of solvent respectively to create a saturated solution. The resulting mixture was then sonicated and allowed to settle for 24 h until the solid and liquid phases reached equilibrium. All solubility measurements were conducted on the supernatant.

To determine the linker solubility in each solvent, 1 mL of supernatant was transferred into a preweighed vial and heated under vacuum at 50 $^{\circ}$ C until only the solid residue remained. This procedure was done to prevent 2-methylimidazole from subliming. The mass of the vial was then weighed to determine the residual mass of the solid. This process was repeated three times to give an average value and standard deviation.

The nanoMOF solubility was determined by thermogravimetric analysis using a TGA Q500, for and each sample 20 μ L of solution was added to the preweighed aluminum TGA pan. The sample was then heated to 10 °C below the boiling point of the solvent to avoid bumping, starting from room temperature at 10 °C/min, and then held isothermally for 15 min while being maintained under constant N₂ flow. The solubility of the nanoMOF was then determined from the residual mass of the TGA curve Figure S13. This process was repeated three times to give an average value and standard deviation.

Solubility after Addition of Excess Solvent or Linker. All sample solubility values were measured as stated above with the following modification: To study the impact of extra solvent, an additional 500 μ L was added to a saturated MeOH solution of 316 nm ZIF-8 particles followed by sonication and allowed to rest for 24 h to reach a new equilibrium. The excess linker measurement followed the same procedure except instead of solvent, 7 mg of 2-methylimidazole was added to solution.

Calculation of Nanoparticle Solubility. To determine MOF solubility in terms of moles of formula units per liter, based on a molecular weight for ZIF-8 of 227.58 g/mol,

mol ZIF-8 = residual mass from TGA (g)
$$\times$$
 227.58 $\frac{g}{mol}$ (S1)

Solubility
$$\left(\frac{mol}{L}\right) = \frac{mol\ ZIF-8}{volume\ pipetted\ into\ pan}$$
 (S2)

To determine the solubility of ZIF-8 in terms of moles of particles per liter, a crystal density of 0.35 g/cm³, molecular weight 227.58 g/mol, and a spherical diameter of 40 nm were assumed:

$$Volume = \frac{4\pi r^3}{3} \tag{S3}$$

Particle M.W. = Volume \times crystal density \times avogadro's number

$$= \frac{g \ particles}{mol}$$
 (S4)

$$mol \ particles = \frac{mass \ from \ TGA}{Particle \ molecular \ weight} \tag{S5}$$

Solubility
$$\left(\frac{mol\ particles}{L}\right) = \frac{mol\ particles}{volume\ pipetted\ for\ TGA}$$
 (S6)

Water Stability of ZIF-8 and ZIF-67. To test the water stability of nanoZIF-8 and ZIF-67 over the 24 h needed to conduct the solubility measurements, a soaking test in Milli-Q water was conducted for 48 h. All solutions were prepared in the same way as those for the solubility measurements. PXRDs were taken for both ZIF-8 and ZIF-67 as both 24 and 48 h Figure S10.

Immersion Calorimetry. Near-room-temperature immersion calorimetry using a microcalorimeter (Setaram C80) was employed to determine the immersion enthalpies of three ZIF-8 samples with different particle sizes in DMF, hexane, and MeOH. In each measurement, ^{30–33} a hand-pressed sample pellet (7–8 mg) was dropped into the organic solvent (8 mL) that was kept at 25 °C in the calorimetry chambers. The direct interactions between the organic

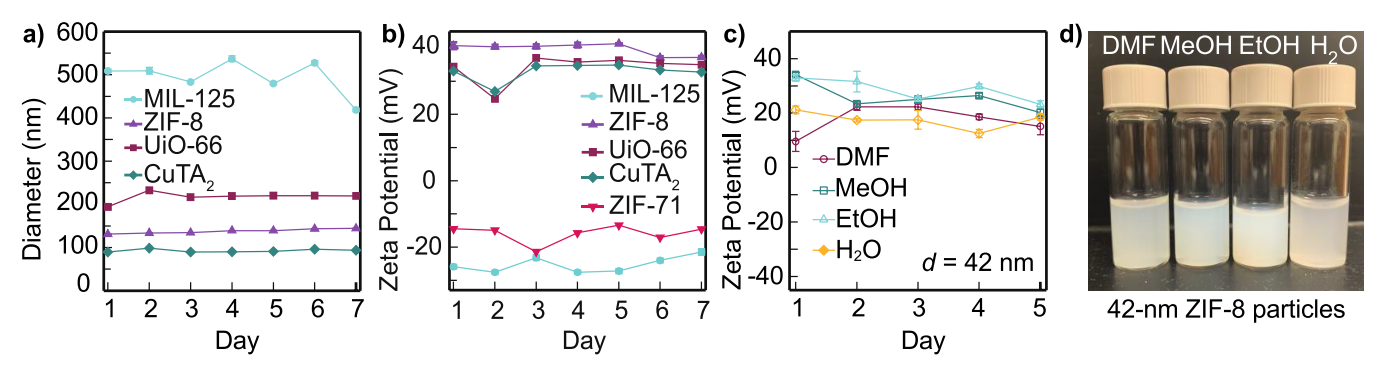


Figure 2. Colloidal stability of nanoMOFs. (A) Nanoparticle hydrodynamic diameter and (B) surface zeta potential measurements of common nanoMOFs suspended in MeOH (1 mg/mL) over a 7-day period. Nanoparticle sizes by Scherrer analysis: 83, 87, 52, and 27 nm, respectively, for MIL-125, ZIF-8, UiO-66, and CuTA₂. (C) Zeta potential measurements of 42 nm crystalline sized nanoZIF-8 suspended in N,N-dimethylformamide (DMF), MeOH (MeOH), ethanol (EtOH), and H_2O . (D) Images of nanoZIF-8 colloids stabilized in DMF, MeOH, EtOH, and H_2O taken 1 month after initial suspension.

solvent and the ZIF-8 sample introduced led to a calorimetric peak. Integration of the area under each calorimetric peak yielded the heat of immersion (kJ) for each ZIF-8 pellet. At least four successful measurements were performed on each sample to ensure reproducibility. The error bars were calculated as two standard deviations of the mean. The average molar formula of ZIF-8 was taken as $C_8H_{10}N_4Zn$ (227.6 g/mol). Immersion calorimetry results are shown in Table S1.

Molecular Dynamics Simulations. Initial Configurations. Atomistic molecular dynamics (MD) simulations were carried out to obtain atomic-scale insights into the experimental observations with four different solvents (Figure S14). A slab of periodic ZIF-8 was placed along the z-axis with the dimensions of $45 \times 60 \text{ Å}^2$ and the solvent reservoirs were maintained around 80 Å totaling a box size of $60 \times 60 \times 205 \text{ Å}^3$. Structural information for ZIF-8 was extracted from crystal structures as reported in Park et al.,8 and the slab was created with VESTA. 9,10 The initial configurations of the solvent systems were generated using Packmol¹¹ with the aid of Molcontroller¹² and VMD.¹³ All MD simulations were carried out using the GROMACS 2020 software package. 14 The OPLS-AA (optimized potential for liquid simulations-all atom)¹⁵ force field parameters were obtained using the LigParGen server 16 and multiple literature sources with partial charges derived from the electrostatic potential (ESP) method. 17-23 (DFT) calculations were performed at ωB97XD/aug-cc-PVDZ level of theory using Gaussian 16 software suite.24

Simulation Details. MD simulations were carried out using the Gromacs 2020 software package.¹⁴ The systems were subject to energy minimization (maximum of 100000 steps) with the steepest descent method followed by 4 ns of NVT (constant number of molecules, volume, and temperature) ensemble equilibration for 500 ps with the velocity rescaling with a stochastic term with a 0.1 ps coupling constant²⁵ at 298.15 K. Subsequently, two NPT (constant number of molecules, pressure, and temperature) ensemble simulations were conducted: The first applied the Berendsen² barostat for 10 ns to stabilize the volume, while the second followed for 40 ns with Parrinello-Rahman²⁷ barostat with a time step of 2 fs and the same temperature controlling parameters as in the previous step. For all ZIF-8/solvent systems, three-dimensional (xyz) periodic boundary conditions (PBC) with a compressibility of $4.5 \times 10^5 \text{ bar}^{-1}$ and a coupling time of 2.0 ps were applied with VdW and particlemesh Ewald (PME)²⁸ cut-offs of 1.4 nm for long-range interactions. Bonds, angles, and dihedrals were constrained during simulations using LINear Constraint Solver (LINCS) algorithm.²

■ RESULTS AND DISCUSSION

Recent literature has revealed preliminary evidence that nanoMOFs exhibit surprising colloidal stability in polar solvents and in the absence of common surfactant

ligands, 12,14,34-36 whereas stability in nonpolar solvents requires careful surface functionalization. 36,37 To investigate the origin of this stability, nanoparticles of five common MOF materials were synthesized and studied for colloidal stability over a week-long period (Figure 2). In certain cases (ZIF-8 and UiO-66) synthetic methods were previously reported. 29,38 while others (CuTA₂ and MIL-125) required novel methods in our laboratories. Dynamic light scattering measurements of MIL-125 (Ti₈O₈(OH)₄(terephthalate)₆), ZIF-8, UiO-66 $(Zr_6O_4(OH)_4(terephthalate)_6)$, and $CuTA_2$ (Cu(1,2,3-triazolate)2) nanoparticles suspended in MeOH exhibited constant hydrodynamic diameters (sizes) over 7 days indicating the nanoparticles avoid aggregation despite the absence of detectable surface ligands or surfactants (as determined by thermogravimetric analysis (TGA) and NMR) (Figure 2a). For comparison with ZIF-8, ZIF-71 (Zn(4,5-dichloroimidazolate)2) nanoparticles were suspended in MeOH and investigated, but due to significantly larger hydrodynamic diameters, they were omitted from Figure 2a and included in Figure S9. In addition to hydrodynamic radii, zeta potentials of all nanoMOFs remained similarly consistent over a week (Figure 2b). The values of these zeta potentials reflect that surface potentials of ±20 mV and larger correlate with long-term colloidal stability of the particles in general.^{39,40} We interpret the positive values of CuTA2, ZIF-8, and UiO-66 to suggest open metal sites dominate their surfaces, while an excess of deprotonated linkers at the surface ZIF-71 and MIL-125 could explain their negative zeta potentials. The stability of these common nanoMOFs with sizes as small as 27 nm is unusual given that metal or conventional semiconductor nanocrystals of similar sizes would quickly aggregate without surface ligands.

Among the investigated nanoMOFs, ZIF-8 nanoparticles exhibit colloidal stability in the widest range of solvents. However, as opposed to conventional quantum dot colloids that suspend in toluene or hexanes following postsynthetic treatment with surfactant molecules, ZIF-8 nanoparticles suspend indefinitely without deliberate surface functionalization in MeOH (MeOH), ethanol (EtOH), water (H₂O), and dimethylformamide (DMF), but not in hexanes, chloroform, or toluene without appropriate surfactant, as shown recently. To probe whether this curious solvent stability depends on particle size, three sizes of ZIF-8 particles were synthesized and suspended in four different solvents and the corresponding zeta potentials were measured over time (Figures 2c and S10). Particle sizes reported here reflect the particle diameters

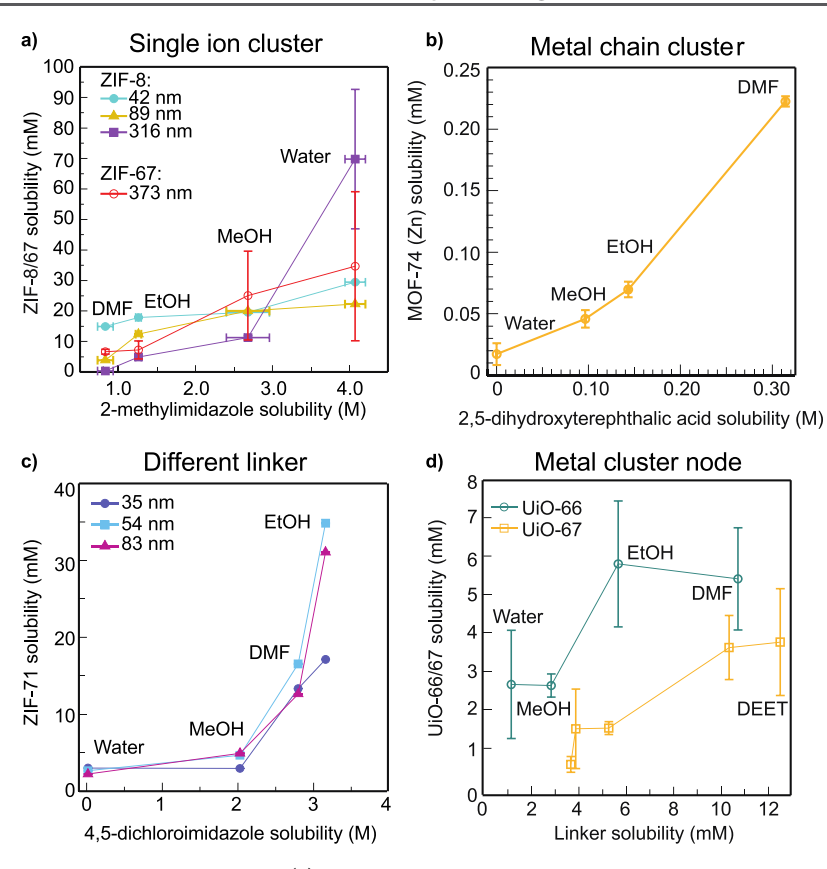


Figure 3. Solvent-dependent linker and particle solubility. (a) Per-formula-unit solubility of ZIF-8 and ZIF-67 particles versus linker solubility. (b) Per-formula-unit solubility of MOF-74 particles versus linker solubility. (c) Per-particle solubility of nanoZIF-71 versus linker solubility. (d) Per-formula-unit solubility of UiO-66 and UiO-67 particles versus linker solubility.

determined from SEM images (Figure S1) as opposed to coherently scattering domain sizes determined by Scherrer analysis of PXRD reflections or hydrodynamic diameters in DMF from dynamic light scattering (DLS) (Figure S18). For all samples, SEM sizes were larger than the values determined by Scherrer and smaller than the hydrodynamic radii. This trend suggests that particles contain multiple crystallite domains. In all solvents, the nanoZIF-8 particles exhibit large and stable zeta potentials, as consistent with DLVO theory that colloids are stabilized by charged surface layers that repel neighboring particles and prevent aggregation. 41-43 Although ZIF-8 particles have been reported to degrade gradually in water, these studies also suggested a strong concentration dependence where more dilute solution degraded faster,⁴⁴ whereas the saturated solutions studied were prepared at far higher concentrations. Furthermore, these nanoZIF-8 methanolic suspensions display visual stability for at least onemonth storage, requiring only gentle sonication (~10 min.) to recover turbid suspensions (Figure 2d). In fact, particles remain stable in methanol with constant zeta potentials of 31 mV for over a year.

Interestingly, the only solvents to suspend ZIF-8 nano-particles are also those that dissolve 2-methylimidazole (2MIm), the linker of ZIF-8. Although one would expect the solvent to etch the particles given the linker solubility, the particles sizes remain constant, as discussed above. Given that linker molecules dominate the atomic composition of ZIF-8, we further explored whether nanoZIF-8 stability arises from favorable interactions with solvent. Using standard solubility methods described in the Supporting Information, the

solubility of 2MIm and nanoZIF-8 were measured in MeOH, EtOH, H2O, and DMF. For the linker 2MIm, solubility was greatest in H2O and lowest in DMF. By solubility, we refer to the maximum quantity of nanoparticles or linker suspended or dissolved at room temperature. Figure 3a plots the solubility of ZIF-8 formula units. These data reveal that particle solubility correlates directly with linker solubility and independent of particle size, given the similarity of solubility of three particle sizes when calculated per-formula-unit. To test whether these measurements truly probe a thermodynamically reversible dissolution-precipitation equilibrium, the solubility was redetermined after 500 µL of additional MeOH was added to methanolic solution of 316 nm ZIF-8 particles. Indeed, gravimetric concentration remained essentially unchanged from $0.4796 \pm 0.1 \text{ mg/mL}$ to $0.4160 \pm 0.05 \text{ mg/mL}$. These results suggest precipitated particles redissolved as expected for a reversible process. To further probe the potential influence of linker-solvent interactions on ZIF-8 nanoparticle solubility, a large excess of 2-mIm was added to a saturated solution of 316 nm particles, causing maximum solubility to raise from 1.294 \pm 0.55 to 6.245 ± 0.8 mg/mL. Because solubility determination involves heating the particles well past the sublimation point of the linker, these results imply precipitated particles redissolve in the presence of excess linker.

To further investigate the origin of ZIF-8 nanoparticle solubility, we measured the solubility of related materials. Figure 3a includes the solubility of nanoZIF-67—a Co²⁺ rather than Zn²⁺ derivative of nanoZIF-8 (Figure 1). These data show solubility sits within the uncertainty of the nanoZIF-8, suggesting solvent—metal site interactions have little impact

on particle solubility. Because ZIF materials contain single-ion clusters, whereas most MOFs feature multinuclear nodes, we explored the solubility of 26 nm MOF-74 (Zn₂(2,5dihydroxyterephthalate)) nanoparticles, which has 1-D metaloxo chains. As shown in Figure 3b, the particles were again most soluble in solvents that best dissolved the linker. To further explore the impact of linker identity on particle solubility, we tested the solubility of nanoZIF-71—a MOF similar to ZIF-8 but composed of a different linker, 4,5dichloroimidazolate (dcIm). Due to the more polar nature of dcIm, the overall solubility trend differed from nanoZIF-8, but the dependence of particle solubility on linker solubility still held, as shown in Figure 3c. With dcIm being now the least soluble in water and the most soluble in ethanol, the solubility of nanoZIF-71 followed the same trend as nanoZIF-8. To explore whether this relationship between particle and linker solubility held for framework materials with discrete multinuclear metal clusters, we measured the solubility of UiO-66 (Zr₆O₄OH₄(1,4-benzenedicarboxylate)₆) (Figure 1) particles and compared against the solubility of the constituent linkers, terephthalate. Indeed, the relationship holds for solvents that dissolve the linker, whereas hexanes, toluene, and other solvents that do not dissolve terephthalic acid also fail to dissolve UiO-66 nanoparticles. Interestingly, nanoMOF performula unit solubility falls in the range of mM for both ZIFs and UiO-66, although the solubility and crystal density of the latter (1.237 g/cm³) are smaller. To further explore the impact of crystal density, linker identity, and pore size, an isoreticular MOF, UiO-67 $(Zr_6O_4OH_4(biphenyl-4,4'-dicarboxylate)_6)$ (Figure 1), was studied. Figure 3d shows that the particle solubility correlates with the solubility of biphenyl-4,4'dicarboxylic acid and is slightly lower than UiO-66 nanoparticle solubility. The lower solubility and crystal density (0.8872 g/cm³) of nanoUiO-67 suggest particle solubility increases when more solvent-linker interactions are available per formula unit. The ability of N₁N-diethyl-meta-toluamide (DEET) to solvate nanoMOFs was also explored given its chemical similarity to DMF but larger size (ca. 10 Å). Interestingly, although DEET dissolves terephthalic acid, it fails to form stable suspensions of UiO-66 (pore sizes are ca. 7.5 and 12 Å), whereas it dissolves both biphenyl-4,4'dicarboxylic acid and UiO-67 (pore sizes are ca. 12 and 16 Å). DEET also fails to form stable suspensions of the smaller pore nanoMOFs of ZIF-8 (3.4 and 11.6 Å), ZIF-67 (3.4 and 11.6 Å), ZIF-71 (4.2 and 16.5 Å), or $Cu(TA)_2$ (4.86 Å). Because calculating molarity depends on assuming the crystal density of the nanoMOF, which might be altered by defects such as collapsed pores or missing constituents, all solubility values for the aforementioned were also plotted simply in g/L units in Figure S14, revealing the same qualitative correlations.

Whereas nanoMOFs generally suspend only in polar solvents, industrial processing of colloidal nanocrystals requires nonpolar suspensions. Therefore, to demonstrate the ability to predict nanoMOF colloidal stability from linker solubility and to achieve nonpolar dispersions of nanoMOFs, we identified ZIF-11 (Zn(benzimidazolate)₂) as a possible candidate due to the slight solubility of the linker in toluene (5.4 \pm 0.9 mM). Indeed, particles of ZIF-11 disperse in toluene with a zeta potential of -5.3 mV.

For insight into the energetics of solvent—nanoMOF interactions, immersion enthalpies of ZIF-8 nanoparticles of different sizes were measured in MeOH and DMF using near-room-temperature immersion calorimetry (Table S1). We

report immersion enthalpies in terms of moles of 2MIm to explore the correlations discussed above between particle solubility and various solvent properties. Immersion of 86.7 nm ZIF-8 in DMF and MeOH gives enthalpies of $-9.6~\rm kJ/mol$ 2MIm and $-8.8~\rm kJ/mol$ 2MIm (Figure 4), respectively, which

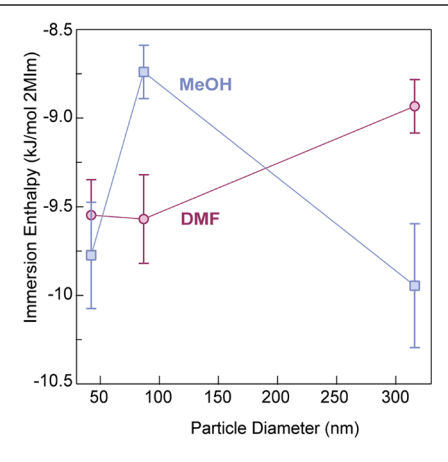


Figure 4. Immersion enthalpies of ZIF-8 particles calculated per mole of 2MIm sites in MeOH or DMF versus particle diameter.

resemble the molar solvation enthalpy of -12.5 ± 0.5 kJ/mol reported for 2-methylimidazole in MeOH at 298 K.46 differently, the solvent environment around 2MIm in bulk solvent resembles the energetics of its environment in ZIF-8 immersed in solvent. These measurements comprise some of the only immersion enthalpies reported for nanocrystals. Immersion enthalpy does not change significantly between different sized particles, however, ranging between -9.0 kJ/ mol 2MIm and -9.6 kJ/mol 2MIm of the largest and smallest particles of ZIF-8 suspended in DMF. When normalizing per mole of Zn sites, these values double to \sim -20 kJ/mol Zn, which is far lower than the ~-80 kJ/mol Zn expected for solvation of Zn²⁺ ions in comparable solvents and the enthalpy of DMF to the open Zn²⁺ sites in MOF-5.⁴⁷ These relatively small enthalpies may also indicate that entropy plays an important role in nanoMOF colloidal stability, just as entropy dominates the solvation energetics of polymers, according to Flory-Huggins theory, 48 and the colloidal stability of proteins. 49,50 Nevertheless, the favorable enthalpy of immersion in polar solvents corroborates the existence of stabilizing solvent-based interactions that contribute to nanoZIF-8 colloidal stability. The size-independence of the values also suggests that particle solubility is not controlled exclusively by solvent interactions, for example with open metal sites, at the external particle surface. Instead, as with polymers, the energetics of MOF particle solubility depend on the sumtotal of all solvent-constituent interactions. Due to the potential availability of both exterior and interior surface in MOF particles, solubility becomes most favorable when solvent gains access to the entire MOF particle, just as how polymer solubility increases when all monomer components are accessible to solvent. However, based on this interpretation, MOF particles may still be soluble if solvent only accesses exterior surfaces, but not as soluble as if interior components could be accessed as well.

For atomic-scale insight into these favorable solvent—MOF interactions, a model system was investigated that simulated bulk solvent interfaced with a well-defined "slab" of ZIF-8, as detailed in Figure S14. Atomistic MD simulations were

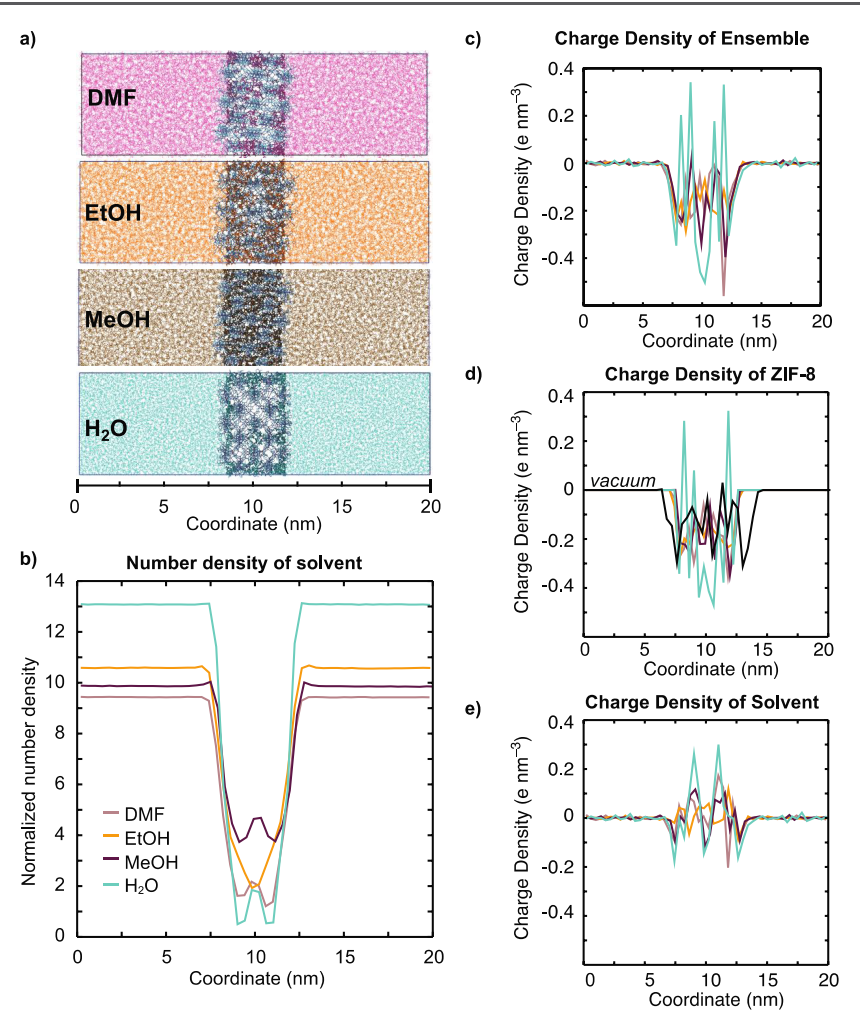


Figure 5. (a) Snapshots from the MD simulations of the four different ZIF-8/solvent systems, (b) solvent number and (c) charge density plots across the long-axes of the ZIF-8/solvent simulation boxes, (d) charge density of ZIF-8, and (e) charge density of the solvents. The number density and charge density values on the *y*-axes represent the numbers of molecules and sums of partial charges, respectively, per 4 Å-wide slices along the *z*-axis.

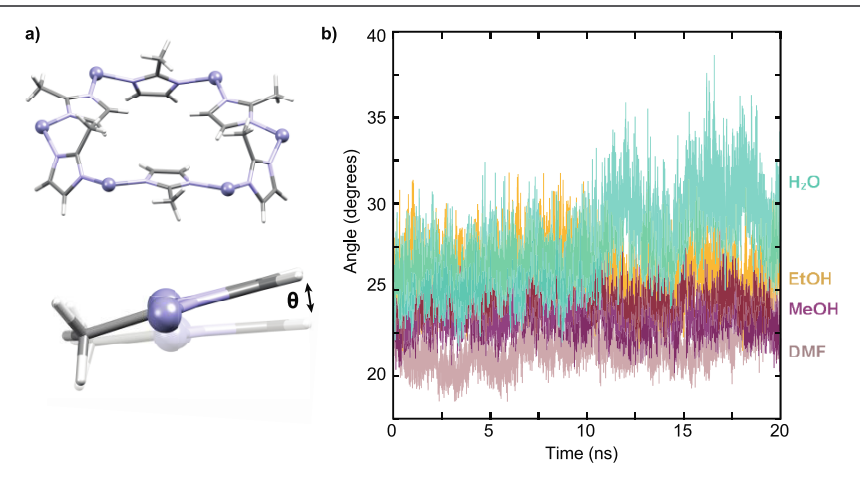


Figure 6. Average angle (θ) of the imidazole ring plane to its initial geometrical position as a function of time. (a) Three-dimensional structure of the aperture of the ZIF-8 molecular pore and angle (θ) between the initial and current geometrical positions. (b) Change in angle with respect to time sampled over the last 20 ns of the NPT simulation.

performed using DMF, EtOH, MeOH, and H₂O and analyzed in terms of the trajectories of the solvent into the slab, the packing density and geometric ordering of solvent within the MOF pores, and the interactions between solvent and ZIF-8

linkers. Figure 5a shows a snapshot of each system after a 50 ns simulation period. Visual inspection indicates that while solvent diffuses into ZIF-8 in all cases, packing density is lower for DMF and H_2O . Figure 5b depicts this result

quantitatively as normalized (dividing by the density of the respective solvent) number density projected along the z-axis of the simulation box, showing H₂O and DMF to have the lowest densities within the ZIF-8 slab and MeOH the highest. With the exception of H₂O, this result suggests the solubility of ZIF-8 depends on the ability of solvent to densely pack inside the pores, which corroborates the solubility versus solvent density trend plotted in Figure 5b. The low packing density of H₂O is expected given its high polarity and the hydrophobic nature of ZIF-8 pores. Although H2O intercalates the least, charge density analysis suggests it interacts the strongest with the MOF interior (Figure 5c-e). A net-zero charge density arises from an isotropic distribution of molecules, as expected for a disordered system such as bulk solvent. The nonzero charge densities shown for the total solvent-ZIF-8 system (Figure 5c), only ZIF-8 (Figure 5d), and only solvent (Figure 5e) indicate that the presence of solvent inside ZIF-8 causes of net reordering of both the MOF and solvent within the pores. Interestingly, the charge density amplitudes are greatest for H₂O. This result suggests that the strong solvating strength of H₂O arises from enthalpically favorable interactions with 2MIm that also contribute to the high solubility of 2MIm in H₂O. Plotted differently as radial distribution distances of solvent with respect to the Zn or N atoms within ZIF-8, Figure S15 reveals that solvent molecules order within the pores as clusters, seen as well-defined peaks and valleys. Regardless of solvent type, the radial distributions show solvent ordering closer to 2MIm than to the metal sites, further supporting experimental evidence of strong solvent-linker interactions.

For insight into how solvents interact differently with 2MIm, we inspected the dynamics of the 2MIm linkers over the course of the simulation. To explain the nonzero charge density of ZIF-8, we suspected solvent induced the "gate-opening" phenomena observed for ZIF-8 and other MOFs with linkers that freely rotate. ^{51–57} Figure 6 plots the average angle change in the imidazole ring plane over the course of the simulation period. ⁵⁸ While linker rotation dynamics are observed for all solvents, the presence of H_2O causes the clearest evidence of net ordering of 2MIm. This result helps to explain the origin of nonzero charge density and provides a rationale for the high solubility of ZIF-8 particles in H_2O despite its low density within the pores.

CONCLUSION

These combined experimental-computational results portray a mechanism of colloidal stability with nanoMOF particles that more closely resembles the solubility of large macromolecules, dictated by exothermic interactions between solvent and the MOF interiors and exteriors. Solubility measurements with varying particle size and composition and immersion calorimetry suggest the solvent-linker energetics dominate these favorable interactions. Although smaller particles have more exposed exterior surface sites, the independence of solubility from particle size suggests that solvent access to the entire particle, including the interior, dominates overall solubility. These results also suggest a positive correlation between the solubility of MOF particles and the solubility of the constituent linker molecules, due to solvent-linker interactions dictating overall particle solubility. Atomistic MD simulations of ZIF-8 interfaced with various solvents suggest that solvents better at packing into the MOF pores lead to greater nanoMOF solubility, further improved by strong solvent-linker interactions. Because solvent can penetrate the

interior cavities and interact with the external surfaces, these results challenge conventional notions of colloidal stability rooted in electrostatic repulsion and surface capping ligands and concepts of solubility reserved for much smaller species. More broadly, these results will improve the solution processability of MOF materials into membranes and thin films for industrial applications.

ASSOCIATED CONTENT

Supporting Information

The Supporting Information is available free of charge at https://pubs.acs.org/doi/10.1021/acs.chemmater.3c03191.

Scanning electron microscope images, powder X-ray diffraction patterns, dynamic light scattering size distributions, thermogravimetric analysis traces, tabulated immersion enthalpy values, and computed solvent radial distribution functions (PDF)

AUTHOR INFORMATION

Corresponding Author

Carl K. Brozek – Department of Chemistry and Biochemistry, Materials Science Institute, University of Oregon, Eugene, Oregon 97403, United States; oorcid.org/0000-0002-8014-7904; Email: cbrozek@uoregon.edu

Authors

- Michael A. LeRoy Department of Chemistry and Biochemistry, Materials Science Institute, University of Oregon, Eugene, Oregon 97403, United States; orcid.org/ 0000-0002-7715-7685
- Anton S. Perera Department of Chemistry & Center for Applied Energy Research, University of Kentucky, Lexington, Kentucky 40506-0055, United States; orcid.org/0000-0003-0596-9403
- Shasanka Lamichhane Department of Chemistry & Center for Applied Energy Research, University of Kentucky, Lexington, Kentucky 40506-0055, United States
- Ashley N. Mapile Department of Chemistry and Biochemistry, Materials Science Institute, University of Oregon, Eugene, Oregon 97403, United States; orcid.org/ 0000-0002-7808-4692
- Faiqa Khaliq Department of Chemistry and Biochemistry, Materials Science Institute, University of Oregon, Eugene, Oregon 97403, United States; orcid.org/0009-0002-1996-1832
- Kentaro Kadota Department of Chemistry and Biochemistry, Materials Science Institute, University of Oregon, Eugene, Oregon 97403, United States
- Xianghui Zhang The Gene and Linda Voiland School of Chemical Engineering and Bioengineering, Washington State University, Pullman, Washington 99164, United States
- Su Ha The Gene and Linda Voiland School of Chemical Engineering and Bioengineering, Washington State University, Pullman, Washington 99164, United States
- Racheal Fisher Department of Chemistry and Biochemistry, Materials Science Institute, University of Oregon, Eugene, Oregon 97403, United States; orcid.org/0000-0002-5445-9832
- Di Wu − The Gene and Linda Voiland School of Chemical Engineering and Bioengineering, Washington State University, Pullman, Washington 99164, United States; orcid.org/ 0000-0001-6879-321X

Chad Risko — Department of Chemistry & Center for Applied Energy Research, University of Kentucky, Lexington, Kentucky 40506-0055, United States; orcid.org/0000-0001-9838-5233

Complete contact information is available at: https://pubs.acs.org/10.1021/acs.chemmater.3c03191

Notes

The authors declare no competing financial interest.

ACKNOWLEDGMENTS

This work made use of the CAMCOR facility of the Lorry I. Lokey Laboratories at the University of Oregon to perform SEM experiments. This material is based upon work supported by the National Science Foundation through the Division of Materials Research under Grant No. DMR-2114430. C.K.B. acknowledges the Research Corporation for Science Advancement for a Cottrell Award. D.W. acknowledges the institutional funds from the Gene and Linda Voiland School of Chemical Engineering and Bioengineering and Alexandra Navrotsky Institute for Experimental Thermodynamics at Washington State University. A.S.P., S.L., and C.R. acknowledge support from the National Science Foundation (NSF) under Cooperative Agreement Number 2019574, and the University of Kentucky (UK) Center for Computational Sciences and Information Technology Services Research Computing for use of the Lipscomb Compute Cluster and associated research computing resources. We gratefully acknowledge insightful conversations with Prof. David C. Johnson.

■ REFERENCES

- (1) Phan, H. T.; Haes, A. J. What Does Nanoparticle Stability Mean? *J. Phys. Chem. C* **2019**, 123 (27), 16495–16507.
- (2) Klajn, R.; Bishop, K. J. M.; Grzybowski, B. A. Light-Controlled Self-Assembly of Reversible and Irreversible Nanoparticle Suprastructures. *Proc. Natl. Acad. Sci. U. S. A.* **2007**, *104* (25), 10305–10309.
- (3) Michelson, A.; Minevich, B.; Emamy, H.; Huang, X.; Chu, Y. S.; Yan, H.; Gang, O. Three-Dimensional Visualization of Nanoparticle Lattices and Multimaterial Frameworks. *Science* **2022**, *376* (6589), 203–207.
- (4) Bischoff, M.; Biriukov, D.; Předota, M.; Roke, S.; Marchioro, A. Surface Potential and Interfacial Water Order at the Amorphous TiO₂ Nanoparticle/Aqueous Interface. *J. Phys. Chem. C* **2020**, *124* (20), 10961–10974.
- (5) Kim, M.; Jeong, J.; Lu, H.; Lee, T. K.; Eickemeyer, F. T.; Liu, Y.; Choi, I. W.; Choi, S. J.; Jo, Y.; Kim, H.-B.; Mo, S.-I.; Kim, Y.-K.; Lee, H.; An, N. G.; Cho, S.; Tress, W. R.; Zakeeruddin, S. M.; Hagfeldt, A.; Kim, J. Y.; Grätzel, M.; Kim, D. S. Conformal Quantum Dot—SnO₂ Layers as Electron Transporters for Efficient Perovskite Solar Cells. *Science* 2022, 375 (6578), 302—306.
- (6) Zhu, W.; Satterthwaite, P. F.; Jastrzebska-Perfect, P.; Brenes, R.; Niroui, F. Nanoparticle Contact Printing with Interfacial Engineering for Deterministic Integration into Functional Structures. *Sci. Adv.* **2022**, *8* (43), No. eabq4869.
- (7) Howes, P. D.; Chandrawati, R.; Stevens, M. M. Colloidal Nanoparticles as Advanced Biological Sensors. *Science* **2014**, *346* (6205), No. 1247390.
- (8) Park, K. S.; Ni, Z.; Cote, A. P.; Choi, J. Y.; Huang, R.; Uribe-Romo, F. J.; Chae, H. K.; O'Keeffe, M.; Yaghi, O. M. Exceptional chemical and thermal stability of zeolitic imidazolate frameworks. *PNAS* **2006**, *103*, 10186–10191.
- (9) Bachman, J. E.; Smith, Z. P.; Li, T.; Xu, T.; Long, J. R. Enhanced Ethylene Separation and Plasticization Resistance in Polymer

- Membranes Incorporating Metal-Organic Framework Nanocrystals. *Nat. Mater.* **2016**, *15* (8), 845–849.
- (10) Erdosy, D. P.; Wenny, M. B.; Cho, J.; DelRe, C.; Walter, M. V.; Jiménez-Ángeles, F.; Qiao, B.; Sanchez, R.; Peng, Y.; Polizzotti, B. D.; de la Cruz, M. O.; Mason, J. A. Microporous Water with High Gas Solubilities. *Nature* **2022**, *608* (7924), 712–718.
- (11) Suresh, K.; Aulakh, D.; Purewal, J.; Siegel, D. J.; Veenstra, M.; Matzger, A. J. Optimizing Hydrogen Storage in MOFs through Engineering of Crystal Morphology and Control of Crystal Size. *J. Am. Chem. Soc.* **2021**, *143* (28), 10727–10734.
- (12) Marshall, C. R.; Staudhammer, S. A.; Brozek, C. K. Size Control over Metal—Organic Framework Porous Nanocrystals. *Chem. Sci.* **2019**, *10* (41), 9396—9408.
- (13) Pappas, N. S.; Mason, J. A. Effect of Modulator Ligands on the Growth of Co₂(Dobdc) Nanorods. *Chem. Sci.* **2023**, *14*, 4647.
- (14) Marshall, C. R.; Dvorak, J. P.; Twight, L. P.; Chen, L.; Kadota, K.; Andreeva, A. B.; Overland, A. E.; Ericson, T.; Cozzolino, A. F.; Brozek, C. K. Size-Dependent Properties of Solution-Processable Conductive MOF Nanocrystals. *J. Am. Chem. Soc.* **2022**, *144* (13), 5784–5794.
- (15) Decker, G. E.; Stillman, Z.; Attia, L.; Fromen, C. A.; Bloch, E. D. Controlling Size, Defectiveness, and Fluorescence in Nanoparticle UiO-66 through Water and Ligand Modulation. *Chem. Mater.* **2019**, 31 (13), 4831–4839.
- (16) Marshall, C. R.; Timmel, E. E.; Staudhammer, S. A.; Brozek, C. K. Experimental Evidence for a General Model of Modulated MOF Nanoparticle Growth. *Chem. Sci.* **2020**, *11* (42), 11539–11547.
- (17) Nag, A.; Kovalenko, M. V.; Lee, J.-S.; Liu, W.; Spokoyny, B.; Talapin, D. V. Metal-Free Inorganic Ligands for Colloidal Nanocrystals: S²⁻, HS⁻, Se²⁻, HSe⁻, Te²⁻, HTe⁻, TeS₃²⁻, OH⁻, and NH₂⁻ as Surface Ligands. *J. Am. Chem. Soc.* **2011**, *133* (27), 10612–10620.
- (18) Yakin, F. E.; Barisik, M.; Sen, T. Pore Size and Porosity Dependent Zeta Potentials of Mesoporous Silica Nanoparticles. *J. Phys. Chem. C* **2020**, *124* (36), 19579–19587.
- (19) Derjaguin, B. V.; Landau, L. Theory of the Stability of Strongly Charged Lyophobic Sols and of the Adhesion of Strongly Charged Particles in Solutions of Electrolytes. *Acta Physicochim. URSS* **1941**, 14. 633–662.
- (20) Verwey, E. J. W. Theory of the Stability of Lyophobic Colloids. *J. Phys. Colloid Chem.* **1947**, *51* (3), 631–636.
- (21) Verwey, E. J. W.; Overbeek, J. Th. G. Theory of the Stability of Lyophobic Colloids; Elsevier: Amsterdam, 1948.
- (22) Yamamoto, E.; Kitahara, M.; Tsumura, T.; Kuroda, K. Preparation of Size-Controlled Monodisperse Colloidal Mesoporous Silica Nanoparticles and Fabrication of Colloidal Crystals. *Chem. Mater.* **2014**, 26 (9), 2927–2933.
- (23) Bouchoucha, M.; Côté, M.-F.; C.-Gaudreault, R.; Fortin, M.-A.; Kleitz, F. Size-Controlled Functionalized Mesoporous Silica Nanoparticles for Tunable Drug Release and Enhanced Anti-Tumoral Activity. *Chem. Mater.* **2016**, 28 (12), 4243–4258.
- (24) Yang, Y.; Qin, H.; Jiang, M.; Lin, L.; Fu, T.; Dai, X.; Zhang, Z.; Niu, Y.; Cao, H.; Jin, Y.; Zhao, F.; Peng, X. Entropic Ligands for Nanocrystals: From Unexpected Solution Properties to Outstanding Processability. *Nano Lett.* **2016**, *16* (4), 2133–2138.
- (25) Guo, A.; Ban, Y.; Yang, K.; Yang, W. Metal-Organic Framework-Based Mixed Matrix Membranes: Synergetic Effect of Adsorption and Diffusion for CO₂/CH₄ Separation. *J. Membr. Sci.* **2018**, 562, 76–84.
- (26) Lin, R.; Villacorta Hernandez, B.; Ge, L.; Zhu, Z. Metal Organic Framework Based Mixed Matrix Membranes: An Overview on Filler/Polymer Interfaces. *J. Mater. Chem. A* **2018**, 6 (2), 293–312.
- (27) Datta, S. J.; Mayoral, A.; Murthy Srivatsa Bettahalli, N.; Bhatt, P. M.; Karunakaran, M.; Carja, I. D.; Fan, D.; Graziane M. Mileo, P.; Semino, R.; Maurin, G.; Terasaki, O.; Eddaoudi, M. Rational Design of Mixed-Matrix Metal-Organic Framework Membranes for Molecular Separations. *Science* **2022**, *376* (6597), 1080–1087.
- (28) DelRe, C.; Hong, H.; Wenny, M. B.; Erdosy, D. P.; Cho, J.; Lee, B.; Mason, J. A. Design Principles for Using Amphiphilic Polymers To

- Create Microporous Water. J. Am. Chem. Soc. 2023, 145 (36), 19982-19988.
- (29) Cravillon, J.; Münzer, S.; Lohmeier, S.-J.; Feldhoff, A.; Huber, K.; Wiebcke, M. Rapid Room-Temperature Synthesis and Characterization of Nanocrystals of a Prototypical Zeolitic Imidazolate Framework. *Chem. Mater.* **2009**, *21* (8), 1410–1412.
- (30) Wu, D.; Navrotsky, A. Small Molecule Silica Interactions in Porous Silica Structures. *Geochim. Cosmochim. Acta* **2013**, *109*, 38–50.
- (31) Quan, Z.; Wu, D.; Zhu, J.; Evers, W. H.; Boncella, J. M.; Siebbeles, L. D. A.; Wang, Z.; Navrotsky, A.; Xu, H. Energy Landscape of Self-Assembled Superlattices of PbSe Nanocrystals. *Proc. Natl. Acad. Sci. U. S. A.* **2014**, *111* (25), 9054–9057.
- (32) Zhang, X.; Cockreham, C. B.; Yılmaz, E.; Li, G.; Li, N.; Ha, S.; Fu, L.; Qi, J.; Xu, H.; Wu, D. Energetic Cost for Being "Redox-Site-Rich" in Pseudocapacitive Energy Storage with Nickel—Aluminum Layered Double Hydroxide Materials. *J. Phys. Chem. Lett.* **2020**, *11* (9), 3745—3753.
- (33) Li, G.; Sun, H.; Xu, H.; Guo, X.; Wu, D. Probing the Energetics of Molecule—Material Interactions at Interfaces and in Nanopores. *J. Phys. Chem. C* **2017**, *121* (47), 26141–26154.
- (34) Troyano, J.; Carné-Sánchez, A.; Avci, C.; Imaz, I.; Maspoch, D. Colloidal Metal—Organic Framework Particles: The Pioneering Case of ZIF-8. *Chem. Soc. Rev.* **2019**, 48 (23), 5534–5546.
- (35) Morris, W.; Wang, S.; Cho, D.; Auyeung, E.; Li, P.; Farha, O. K.; Mirkin, C. A. Role of Modulators in Controlling the Colloidal Stability and Polydispersity of the UiO-66 Metal—Organic Framework. *ACS Appl. Mater. Interfaces* **2017**, *9* (39), 33413—33418.
- (36) Yang, X.; Zhang, Q.; Liu, Y.; Nian, M.; Xie, M.; Xie, S.; Yang, Q.; Wang, S.; Wei, H.; Duan, J.; Dong, S.; Xing, H. Metal-Organic Framework Nanoparticles with Universal Dispersibility through Crown Ether Surface Coordination for Phase-Transfer Catalysis and Separation Membranes. *Angew. Chem., Int. Ed.* **2023**, 63, No. e202303280.
- (37) Carey, C. A.; Devlin, A. M.; Matzger, A. J. Dual Modification of MOFs Improves Dispersion and Ionic Conductivity of Mixed Matrix Membranes. *ACS Mater. Lett.* **2024**, *6*, 159–164.
- (38) Schaate, A.; Roy, P.; Godt, A.; Lippke, J.; Waltz, F.; Wiebcke, M.; Behrens, P. Modulated Synthesis of Zr-Based Metal-Organic Frameworks: From Nano to Single Crystals. *Chem. Eur. J.* **2011**, *17* (24), 6643–6651.
- (39) Butler, E. L.; Reid, B.; Luckham, P. F.; Guldin, S.; Livingston, A. G.; Petit, C. Interparticle Forces of a Native and Encapsulated Metal-Organic Framework and Their Effects on Colloidal Dispersion. *ACS Appl. Mater. Interfaces* **2021**, *13* (38), 45898–45906.
- (40) Rojas, S.; Carmona, F. J.; Maldonado, C. R.; Horcajada, P.; Hidalgo, T.; Serre, C.; Navarro, J. A. R.; Barea, E. Nanoscaled Zinc Pyrazolate Metal—Organic Frameworks as Drug-Delivery Systems. *Inorg. Chem.* **2016**, *55* (5), 2650–2663.
- (41) Tran, E.; Richmond, G. L. Interfacial Steric and Molecular Bonding Effects Contributing to the Stability of Neutrally Charged Nanoemulsions. *Langmuir* **2021**, 37 (43), 12643–12653.
- (42) Derjaguin, B. V.; Churaev, N. V.; Muller, V. M. The Derjaguin—Landau—Verwey—Overbeek (DLVO) Theory of Stability of Lyophobic Colloids. In *Surface Forces*; Derjaguin, B. V., Churaev, N. V., Muller, V. M., Eds.; Springer US: Boston, MA, 1987; pp 293–310, .
- (43) Johny, J.; van Halteren, C. E. R.; Zwiehoff, S.; Behrends, C.; Bäumer, C.; Timmermann, B.; Rehbock, C.; Barcikowski, S. Impact of Sterilization on the Colloidal Stability of Ligand-Free Gold Nanoparticles for Biomedical Applications. *Langmuir* **2022**, *38*, 13030.
- (44) Zhang, H.; Zhao, M.; Lin, Y. S. Stability of ZIF-8 in Water under Ambient Conditions. *Microporous Mesoporous Mater.* **2019**, 279, 201–210.
- (45) Talapin, D. V.; Lee, J.-S.; Kovalenko, M. V.; Shevchenko, E. V. Prospects of Colloidal Nanocrystals for Electronic and Optoelectronic Applications. *Chem. Rev.* **2010**, *110* (1), 389–458.
- (46) Herrera-Castro, F.; Torres, L. A. Understanding the Solvation Process and Solute-Solvent Interactions of Imidazole Compounds in

- Three Different Solvents through Solution Calorimetry and ¹H NMR. J. Mol. Liq. 2019, 284, 232–240.
- (47) Akimbekov, Z.; Wu, D.; Brozek, C. K.; Dincă, M.; Navrotsky, A. Thermodynamics of Solvent Interaction with the Metal—Organic Framework MOF-5. *Phys. Chem. Chem. Phys.* **2016**, *18* (2), 1158—1162.
- (48) Flory, P. J. Molecular Size Distribution in Linear Condensation Polymers 1. J. Am. Chem. Soc. 1936, 58 (10), 1877–1885.
- (49) Wennerström, H.; Vallina Estrada, E.; Danielsson, J.; Oliveberg, M. Colloidal Stability of the Living Cell. *Proc. Natl. Acad. Sci. U. S. A.* **2020**, *117* (19), 10113–10121.
- (50) Israelachvili, J. N.; Wennerstroem, H. Entropic Forces between Amphiphilic Surfaces in Liquids. *J. Phys. Chem.* **1992**, *96* (2), 520–531
- (51) Hobday, C. L.; Woodall, C. H.; Lennox, M. J.; Frost, M.; Kamenev, K.; Düren, T.; Morrison, C. A.; Moggach, S. A. Understanding the Adsorption Process in ZIF-8 Using High Pressure Crystallography and Computational Modelling. *Nat. Commun.* **2018**, 9 (1), 1429.
- (52) Tan, J. C.; Bennett, T. D.; Cheetham, A. K. Chemical Structure, Network Topology, and Porosity Effects on the Mechanical Properties of Zeolitic Imidazolate Frameworks. *Proc. Natl. Acad. Sci. U. S. A.* **2010**, *107* (22), 9938–9943.
- (53) Fairen-Jimenez, D.; Moggach, S. A.; Wharmby, M. T.; Wright, P. A.; Parsons, S.; Düren, T. Opening the Gate: Framework Flexibility in ZIF-8 Explored by Experiments and Simulations. *J. Am. Chem. Soc.* **2011**, *1*33 (23), 8900–8902.
- (54) Zheng, B.; Pan, Y.; Lai, Z.; Huang, K.-W. Molecular Dynamics Simulations on Gate Opening in ZIF-8: Identification of Factors for Ethane and Propane Separation. *Langmuir* **2013**, *29* (28), 8865–8872.
- (55) Kolokolov, D. I.; Stepanov, A. G.; Jobic, H. Mobility of the 2-Methylimidazolate Linkers in ZIF-8 Probed by ²H NMR: Saloon Doors for the Guests. *J. Phys. Chem. C* **2015**, *119* (49), 27512–27520.
- (56) Tian, T.; Wharmby, M. T.; Parra, J. B.; Ania, C. O.; Fairen-Jimenez, D. Role of Crystal Size on Swing-Effect and Adsorption Induced Structure Transition of ZIF-8. *Dalton Trans.* **2016**, 45 (16), 6893–6900.
- (57) Coudert, F. Molecular Mechanism of Swing Effect in Zeolitic Imidazolate Framework ZIF-8: Continuous Deformation upon Adsorption. *ChemPhysChem* **2017**, *18* (19), 2732–2738.
- (58) Vitillo, J. G.; Gagliardi, L. Modeling Metal Influence on the Gate Opening in ZIF-8 Materials. *Chem. Mater.* **2021**, 33 (12), 4465–4473.